
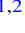



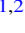




Can Dark Stars Account for the Star Formation Efficiency Excess at Very High Redshifts?

Lei Lei (雷磊)^{1,2} , Yi-Ying Wang (王艺颖)^{1,2} , Guan-Wen Yuan (袁官文)^{3,4} , Tong-Lin Wang (王彤琳)¹ ,
Martin A. T. Groenewegen⁵ , and Yi-Zhong Fan (范一中)^{1,2} 

¹ Key Laboratory of Dark Matter and Space Astronomy, Purple Mountain Observatory, Chinese Academy of Sciences, Nanjing 210023, People's Republic of China; wangyy@pmo.ac.cn, yzfan@pmo.ac.cn

² School of Astronomy and Space Science, University of Science and Technology of China, Hefei 230026, People's Republic of China

³ Department of Physics, University of Trento, Via Sommarive 14, 38123 Povo (TN), Italy

⁴ Trento Institute for Fundamental Physics and Applications (TIFPA)-INFN, Via Sommarive 14, 38123 Povo (TN), Italy

⁵ Royal Observatory of Belgium, Ringlaan 3, 1180 Brussels, Belgium

Received 2024 July 12; revised 2024 December 8; accepted 2025 January 10; published 2025 February 19

Abstract

The James Webb Space Telescope (JWST) has recently conducted observations of massive galaxies at high redshifts, revealing a notable anomaly in their star formation efficiency (SFE). Motivated by the recent identification of three $\sim 10^6 M_\odot$ dark star candidates, we investigate whether dark stars can be the origin of the SFE excess. It turns out that the excess can be reproduced by a group of dark stars with $M \gtrsim 10^3 M_\odot$, because of their domination in generating primary UV radiation in high-redshift galaxies. The genesis of these dark stars is attributed to the capture of weakly interacting massive particles within a mass range of tens of gigaelectronvolts to a few teraelectronvolts. However, if the top-heavy initial mass function of dark stars holds up to $\sim 10^5 M_\odot$, the relic black holes stemming from their collapse would be too abundant to be consistent with the current observations of massive compact halo objects. We thus suggest that just a small fraction of SFE excess may be contributed by the very massive dark stars, with the majority likely originating from other sources, such as the Population III stars, in view of their rather similar UV radiation efficiencies.

Unified Astronomy Thesaurus concepts: [High-redshift galaxies \(734\)](#); [Star formation \(1569\)](#); [Dark matter \(353\)](#); [Supermassive black holes \(1663\)](#)

1. Introduction

The observations by JWST in the high-redshift Universe have posed significant challenges to the prevailing Λ CDM model of galaxy formation (M. Haslbauer et al. 2022; M. Boylan-Kolchin 2023; I. Labbé et al. 2023; N. Menci et al. 2024; J. C. Wang et al. 2024a; M. Xiao et al. 2024). These observations have raised two key challenges for theoretical frameworks explaining galaxy formation: first, the elevated stellar-mass density is observed in JWST high-redshift galaxies at $z > 6$ (M. Boylan-Kolchin 2023; I. Labbé et al. 2023; Colgáin et al. 2024; M. Xiao et al. 2024); and second, the abundance of bright galaxies at $z > 10$ is higher than the prediction of the ultraviolet luminosity functions (UV LFs) under the Λ CDM framework (R. P. Naidu et al. 2022; R. Bouwens et al. 2023; R. J. Bouwens et al. 2023; C. T. Donnan et al. 2023; S. L. Finkelstein et al. 2023; C. C. Lovell et al. 2023; T. Morishita & M. Stiavelli 2023; P. G. Pérez-González et al. 2023; N. J. Adams et al. 2024; Y. Harikane et al. 2024; D. J. McLeod et al. 2024). Both challenges can be attributed to an observed excess in star formation efficiency (SFE). The SFE excesses may be caused by the high formation efficiency of the first stars (or Population III stars) in the early galaxies (K. Inayoshi et al. 2022; L. Y. A. Yung et al. 2024) or several alternative scenarios, such as feedback-free star formation activities (A. Dekel et al. 2023), dust-free star formation activities, or the presence of a stellar top-heavy initial mass function (IMF; S. L. Finkelstein et al. 2023; Y. Harikane et al. 2024) in the early Universe. However,

these alternative models struggle to reconcile the observed high SFE approaching 100% at $z \geq 10$ in JWST observations.

Dark stars, which inhabit the first dark matter (DM) halos or minihalos in the high-redshift Universe, are fueled by heating from DM (K. Freese et al. 2008, 2016; Y. Wu et al. 2022; F. Iocco & L. Visinelli 2024; S. Zhang et al. 2024). This heating may originate from the gravitational attraction of DM and the annihilation of DM particles, such as weakly interacting massive particles (WIMPs), which can be captured through elastic scattering with baryonic matter (K. Freese et al. 2010). In the early Universe, DM densities were enhanced by a factor of $(1+z)^3$ at redshift z , suggesting a condition favoring the formation of dark stars (K. Freese et al. 2016). However, before the launch of JWST, identifying dark stars was challenging, due to the lack of very-high-redshift observations. Moreover, the outer atmospheric properties of dark stars show similar characteristics compared with those of stars undergoing nuclear reactions, enhancing the difficulty of identification. The dark star observational features might include supermassive dark stars (F. Iocco et al. 2008; A. Natarajan et al. 2009; E. Zackrisson et al. 2010a, 2010b; C. Ilie et al. 2012; K. Freese et al. 2016), the extragalactic infrared background light (A. Maurer et al. 2012), the extragalactic gamma-ray background (P. Sandick et al. 2011, 2012; Q. Yuan et al. 2011), remnant black holes following the demise of dark stars (C. Ilie et al. 2023), the influence of dark stars on the Universe's reionization process (D. R. G. Schleicher et al. 2009; P. Scott et al. 2011; P. Gondolo et al. 2022; W. Qin et al. 2024), and so on.

Recently, three potential supermassive dark star candidates have been identified by JWST (C. Ilie et al. 2023), for which the power sources are rooted in the annihilation of DM particles

rather than nuclear fusion (K. Freese et al. 2016). Supposing supermassive dark stars indeed exist, a population of dark stars living within the very-high-redshift galaxies could influence the UV LFs of galaxies. If the light outputs of these dark stars can be comparable with normal stars, the formation and evolution of galaxies will be affected in the early Universe. In this work, we investigate the possible net contribution of the dark stars to the overall SFE.

In Section 2, we model the UV LFs of high-redshift galaxies observed by JWST, considering both dark star and normal star populations. In Section 3, we analyze the abundance of massive compact halo objects (MACHOs) and examine the possibility that they originated from the collapse of dark stars. We then compare the UV LF model with the UV LF data obtained from JWST. Section 4 presents the conclusions and discussions. The cosmological parameters used in this work include $H_0 = 67.36 \text{ km Mpc}^{-1} \text{ s}^{-1}$, $\Omega_m = 0.3135$, and $\Omega_\Lambda = 0.6847$ (Planck Collaboration et al. 2020). The absolute bolometric magnitude system (J. B. Oke & J. E. Gunn 1983) is adopted in this work.

2. Observational Data and Fitting SFE Model

2.1. Observational Data

To avoid the problem of overlapping sky maps, we have carefully selected the high-redshift UV LF data ($9 \geq z \geq 4$) from various sources. These sources encompass data from the Hubble Space Telescope (R. J. Bouwens et al. 2021), the Subaru/Hyper Suprime-Cam survey and CFHT Large Area U -band Survey (Y. Harikane et al. 2022a), the Spitzer/Infrared Array Camera (R. A. A. Bowler et al. 2020), and JWST (C. T. Donnan et al. 2023; T. Morishita & M. Stiavelli 2023; P. G. Pérez-González et al. 2023; N. J. Adams et al. 2024). For higher redshifts ($z \geq 11$), where the luminosity contribution of dark stars is considered in our model, we adopt the UV LF data from relevant JWST literature (Y. Harikane et al. 2022b, 2023; R. Bouwens et al. 2023; R. J. Bouwens et al. 2023; C. T. Donnan et al. 2023; P. G. Pérez-González et al. 2023; C. M. Casey et al. 2024; S. L. Finkelstein et al. 2024; D. J. McLeod et al. 2024). To ensure the reliability and coherence of our data set, we have excluded any candidates identified as low-redshift objects (Y. Y. Wang et al. 2023) and removed samples that are already covered in the JWST deep fields.

2.2. SFE Model

The star formation rate (SFR) can be determined from the UV luminosity using the relation (P. Madau & M. Dickinson 2014)

$$\text{SFR}_{\text{UV}}(M_\odot \text{ yr}^{-1}) = \mathcal{K}_{\text{UV}} \times L_{\text{UV}}(\text{erg s}^{-1} \text{ Hz}^{-1}). \quad (1)$$

Here, \mathcal{K}_{UV} represents the conversion factor, which depends on the stellar populations of galaxies (P. Madau & M. Dickinson 2014). In the standard scenario, this conversion factor takes the value $\mathcal{K}_{\text{UV}} = 1.15 \times 10^{-28} M_\odot \text{ yr}^{-1}/(\text{erg s}^{-1} \text{ Hz}^{-1})$, assuming a Salpeter IMF within the mass range of 0.1–100 M_\odot (E. E. Salpeter 1955). For extremely metal-poor ($Z=0$) Population III stars characterized by a Salpeter IMF spanning 50–500 M_\odot , the reported conversion factor decreases to $2.80 \times 10^{-29} M_\odot \text{ yr}^{-1}/(\text{erg s}^{-1} \text{ Hz}^{-1})$ (K. Inayoshi et al. 2022). In our analysis, we estimate the conversion factor using the mass-to-luminosity ratio of dark stars, assuming a power-

law IMF with $\phi(m) \propto m^{-0.17}$ (see Appendix A for details). We find that the conversion factor for dark stars aligns closely with that of Population III stars. Consequently, we adopt the conversion factor $\mathcal{K}_{\text{UV}} = 2.80 \times 10^{-29} M_\odot \text{ yr}^{-1}/(\text{erg s}^{-1} \text{ Hz}^{-1})$ to fit the UV LF data.

We employ an extensive model of galaxy evolution to analyze the UV LF and explore the evolution of the SFE. The SFR is derived from the accretion rate of baryons and the total SFE, expressed as

$$\text{SFR}_{\text{UV}} = f_{\text{tot}} \times \dot{M}_b, \quad f_{\text{tot}} = f_S + f_{\text{DS}}, \quad (2)$$

where f_S (f_{DS}) represents the SFE of stars (dark stars), and \dot{M}_b is the baryon accretion rate of the galaxy, which can be derived from the accretion rate of the DM halo:

$$\dot{M}_b = f_b \times \dot{M}_h, \quad (3)$$

$$f_b \equiv \frac{\Omega_b}{\Omega_m} = 0.156. \quad (4)$$

The accretion rate of the DM halo \dot{M}_h can be obtained by simulation (P. S. Behroozi & J. Silk 2015).

Due to the differences in physical processes, the formation efficiency of stars f_S and dark stars f_{DS} in Equation (2) may differ in definitions. Observations have indicated that stars form in the dense, cold, molecular phase of the interstellar medium. Current detections support a (nearly) universal low SFE in Equation (5) in the nearby galaxies and indicate that the temperature of dust/gas will influence the SFE. The energy injection from radiation processes like reionization, stellar winds, supernovae, and active galactic nuclei will negatively affect the SFE f_S (R. S. Somerville & R. Davé 2015; R. H. Wechsler & J. L. Tinker 2018). In this work, the SFE f_S is calculated using a parametric formula dependent on the DM halo mass within the extensive model of galaxy evolution (R. H. Wechsler & J. L. Tinker 2018):

$$f_S = \frac{2\epsilon_N}{\left(\frac{M_h}{M_1}\right)^{-\beta} + \left(\frac{M_h}{M_1}\right)^\gamma}. \quad (5)$$

In this expression, ϵ_N denotes the normalized constant, M_1 is the characteristic mass, where the SFE is equal to ϵ_N , M_h is the halo mass, and β, γ are slopes determining the decrease in SFE at low and high masses, respectively. The characteristic mass of the DM halo is set to be $M_1 = 10^{12} M_\odot$, as suggested in Y. Harikane et al. (2022a) and Y. Y. Wang et al. (2023).

However, dark stars are thought to be powered by DM annihilation at the galaxy's center. Therefore, their formation efficiency is likely to be strongly correlated with the mass of the DM halo. Compared with normal stars, the formation efficiency of dark stars is more reliant on the density of DM, which is directly linked to the mass of the DM halo. Given the absence of mature simulations or analytical theories on this topic, it becomes necessary to define a new formation efficiency function specifically for dark stars. For characterizing the formation efficiency of dark stars, we utilize a power-law model, expressed as

$$f_{\text{DS}} = \epsilon_{\text{DS}} \left(\frac{M_h}{M_1}\right)^{\gamma_{\text{DS}}}, \quad (6)$$

where ϵ_{DS} is the normalization constant, M_1 is the characteristic mass, and γ_{DS} is the slope governing the dark star SFE across

different halo masses. As shown in Equation 6, the dark SFE f_{DS} is assumed to have a monotonically incremental relationship with the DM halo mass M_h .

Population III stars are believed to form in low-metallicity gas clouds within DM minihalos (S. Glover 2013; J. L. Johnson 2013; R. S. Klessen & S. C. O. Glover 2023). However, the details need to be better understood, and it is likely that the formation efficiency is related to the mass of the halo. Consequently, we assume that the formation efficiency of Population III stars is analogous to that of dark stars, as outlined in Equation (6). In our analysis, we utilize the conversion factor $\mathcal{K}_{\text{UV}} = 2.80 \times 10^{-29} M_\odot \text{ yr}^{-1} / (\text{erg s}^{-1} \text{ Hz}^{-1})$ for both dark star and Population III SFE models to fit the UV LF data. The primary distinction between the dark stars and Population III stars in this study lies in their IMFs: Population III stars have a mass range of $50 \leq M_* \leq 500 M_\odot$ with a Salpeter IMF $\phi(m) \propto m^{-2.35}$, while dark stars have a mass range exceeding $500 M_\odot$ and follow a top-heavy IMF $\phi(m) \propto m^{+0.17}$.

According to Y. Y. Wang et al. (2023), the theoretical model of UV LFs can be written as

$$\Phi(M_{\text{UV}}) = \phi(M_h) \left| \frac{dM_h}{dM_{\text{UV}}} \right|, \quad (7)$$

where $\left| \frac{dM_h}{dM_{\text{UV}}} \right|$ is the Jacobi matrix mapping from $\phi(M_h)$ to $\Phi(M_{\text{UV}})$, and M_{UV} is the dust-corrected or intrinsic magnitude, depending on whether the dust attenuation effect is considered or not. The halo-mass number density function $\phi(M_h)$ is from the number of DM halos per unit mass per unit comoving volume:

$$\frac{dn}{d \ln M_h} = M_h \cdot \frac{\rho_0}{M_h^2} f(\sigma) \left| \frac{d \ln \sigma}{d \ln M_h} \right|, \quad (8)$$

where ρ_0 is the mean density of the Universe and σ is the rms variance of mass, which is determined by the linear power spectrum and the top-hat window function. The linear power spectrum can be computed using the transfer function provided by the public Code for Anisotropies in the Microwave Background (CAMB; A. Lewis et al. 2000). The mass function $f(\sigma)$ of DM halos is from the high-resolution N -body simulations in D. S. Reed et al. (2007). In detail, $\phi(M_h)$ can be derived by the public package HMFALC (S. G. Murray et al. 2013) conveniently. Assuming M_h distributes over a wide range from 10^2 to $10^{16} M_\odot$ with a tiny bin ($\log_{10} \Delta M_h = 0.01$), the absolute magnitude (M_{UV}) of the corresponding galaxy for each DM halo (M_h) can be derived from Equations (1)–(6). Therefore, the term of $\frac{dM_h}{dM_{\text{UV}}}$ in Equation (7) can be calculated by the differentials of M_h and M_{UV} . After building such a connection between M_h and M_{UV} , the UV LF model can be constructed by Equation (7).

2.3. Fitting Results

All of the variable parameters in Equations (2), (5), and (6) can be estimated by fitting the observations of the UV luminosity functions with Equation (7). In Bayesian analysis, the likelihood function follows an asymmetric normal

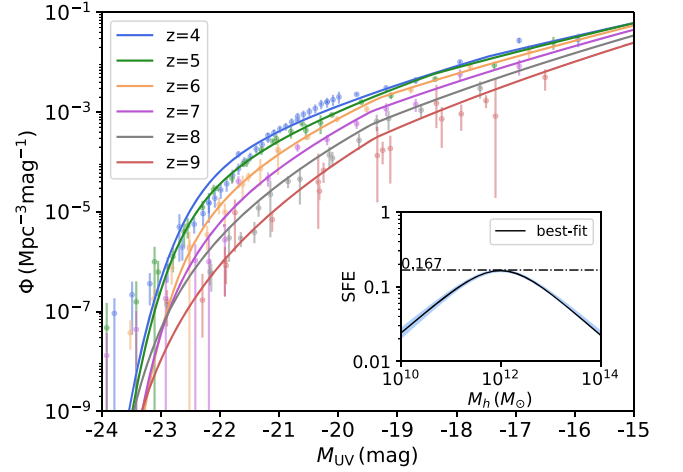


Figure 1. The fitting results of UV LF observations within the redshift range of approximately 4–9. All of the solid lines represent the optimal fits for the complete data set, with data points derived from observations. In the subfigure, the light blue region illustrates the comprehensive posterior distribution of SFE.

distribution because of the asymmetric uncertainties of these real data:

$$\mathcal{L} = \prod_i^N \text{AN}(f(x_i) - y_i | c_i, d_i), \quad (9)$$

where AN is the asymmetric normal distribution, $f(x_i)$ are the observed UV LFs at magnitudes x_i , y_i are the model values, and c_i and d_i represent the deviation and the skewness of the distribution, respectively, which can be obtained from the asymmetric errors of the observation (i.e., Equation (14) of B. Kiziltan et al. 2013). We use the nested sampling method and adopt *Pymultinest* (J. Buchner et al. 2014) as the sampler to calculate the posterior distributions of the parameters. In the *Pymultinest* framework, the comparison of the models is assessed through the computation of the Bayesian evidence, as detailed by F. Feroz et al. (2009) and J. Buchner et al. (2014). The Bayesian evidence, denoted as \mathcal{Z} , is given by the following integral:

$$\mathcal{Z} = \int \mathcal{L}(\Theta) \pi(\Theta) d^D \Theta, \quad (10)$$

where Θ represents the set of parameters within the model, $\pi(\Theta)$ is the prior probability distribution, and D signifies the dimensionality of the parameter space.

In the range of $4 \leq z \leq 9$, we assume a constant ϵ_N value for SFE to estimate the contribution of the Population II star formation. When fitting the UV LFs, we only consider the Population II SFR (i.e., we discard the dark star part of Equation (2): $\text{SFR}_{\text{UV}} = f_S \times \dot{M}_b$, where the Population II SFE f_S is defined by Equation (5)). As shown in Figure 1, the SFE is constrained within a tight range, resulting in the well-fitted UV LFs. Table 1 shows the best-fit values and posterior distributions of the parameters of the Population II SFE model. The best-fit values of the parameters are taken from posteriors corresponding to the maximum likelihood. The 1σ range of the fitting error of the parameter in the tables is the 68% credible level of the posterior distribution. Subsequently, the best-fit values are used to calculate the SFE of Population II stars at $z \geq 10$. The remaining contribution to the SFR is attributed to the formation of dark stars. In Equation (2), we introduce f_{DS} to

Table 1
The Best-fit Values and Posterior Results of the Population II SFE Parameters at $4 \leq z \leq 9$

Redshift	Best-fit Values			Posterior Results at 68% Credible Level			$\ln(\mathcal{Z})$
	ϵ_N	β	γ	ϵ_N	β	γ	
4–9 ^a	0.158	0.564	0.580	$0.157^{+0.001}_{-0.001}$	$0.564^{+0.008}_{-0.008}$	$0.577^{+0.003}_{-0.004}$	1258.46

Note.

^a In the range of $4 \leq z \leq 9$, we fit the data with a Population II SFE, without considering dark stars (or Population III stars).

represent the efficiency of dark star formation. In the analysis, we specifically extrapolate the Population II star formation contribution to the UV LF at redshifts $z \sim 11$ –14 using the fitting results from the redshift range $z \sim 4$ –9. The SFE parameters that describe the contribution of Population II stars are fixed to the best-fit values at $z \sim 4$ –9, which are listed in Table 1. The remaining contributions at $z \sim 11$ –14 are then attributed to dark stars (or Population III stars) and fitted using a power-law model specific to these populations. This method allows us to isolate the contribution of dark stars (or Population III stars) and assess their influence on the UV LF at these elevated redshifts.

Figure 2 shows the UV LF and SFE models at redshifts of $z = 11, 12, 13,$ and 14 . The blue and red bands depict the 68.3% posterior regions of the Population II Star + Dark Star (or Population II + III Star) models, including two cases with and without the effects of dust attenuation, respectively. We also applied the Population II Star + Dark Star model to fit the UV LF at redshifts around $z \sim 10$. However, our results indicate that the SFE of the dark stars (or Population III stars) is a feeble contribution, which is ~ 2 dex lower than other redshifts ($z > 10$). Because the $z \sim 10$ UV LF can be fitted well without the dark stars (or Population III stars), we show the UV LF data and fitted models at $z \sim 11$ –14 in Figure 2. The black dashed-dotted line represents the UV LF model without dark stars (or Population III stars), derived from the best-fitted UV LF model in the redshift bin $z \sim 4$ –9.

The derived model lines are significantly lower than the high-redshift JWST UV LF data, indicating a significant transition from the low- to the high-redshift range. The tension between the UV LF model and the data becomes more pronounced at higher redshifts, reaching approximately ~ 2 dex/ ~ 3 dex at $z \sim 13/z \sim 14$, respectively. Specifically, the bright end of the UV LF exhibits a larger tension in each redshift bin. The Population II Star + Dark Star (or Population II + III Star) scenario provides a good fit for the current data, with dark stars playing a dominant role. The higher UV radiative efficiency of dark stars leads to a lower SFE fitting the UV LF. The posterior distributions of the SFE model can be found in Figure 4 of Appendix B.

Table 2 presents the best-fit values of the dark stars' (or Population III stars') formation parameter and the posterior results of the SFE model parameters. We also plot the corners of the posteriors in Figures 5 and 6 in Appendix B. The dark red regions of the three depths in the corner plots of Figures 5 and 6 represent 68%, 95%, and 99% confidence intervals, respectively. The black crosses are the positions of the best-fit parameters. Even if the best-fit parameter is within the 68% credible interval on the two-dimensional corner plot, the best-fit value of a single parameter may deviate from the 68% credible interval because of the non-Gaussian posterior distribution. The fitted dark star (or Population III star) formation efficiencies, denoted as ϵ_{DS} , for the redshift bins around $z \sim 13$ and $z \sim 14$

are higher than those for the bins around $z \sim 11$ and $z \sim 12$. This trend is in agreement with the UV LF models depicted in Figure 2. However, we also see that the number of UV LF data points for $z \sim 13$ and $z \sim 14$ is very small, so more data are needed for more robust investigations in the future.

The Bayesian evidence is a metric that quantifies the relative fit of two models to the data, with higher values indicating superior performance on the data set. By examining the log-evidence values for the various models presented in Table 2, we are able to assess the impact of including or excluding dust attenuation in our UV LF model fits. The Bayes factor (\mathcal{B}), defined as the ratio of the evidence for two models, is a standard tool for gauging the relative support for one model over another: $\mathcal{B} = \frac{\mathcal{Z}_a}{\mathcal{Z}_b}$. As demonstrated, the differences in the log-evidence values for our models, expressed as $\ln(\mathcal{B}) = \ln(\mathcal{Z}_a) - \ln(\mathcal{Z}_b)$, are less than 1.0 when comparing fits with and without consideration of dust. This suggests that our model fits are robust and not significantly influenced by the inclusion of dust extinction effects, as the Bayes factors do not exceed 3, indicating no strong evidence in favor of one model over the other.

3. Constraint of MACHOs from Dark Stars' Collapse

According to the observations summarized in M. Volonteri et al. (2021), there are two key facts regarding the low spatial density of massive black holes in the Universe: (1) the local Universe's abundance of massive black holes is estimated to be $n_{BH} \sim 0.01$ – 0.001 Mpc^{-3} , which is relatively low compared to the population of stars (also see J. E. Greene et al. 2020); and (2) luminous quasars at redshifts around $z \sim 6$ are quite rare, with a density of $n_{BH} \sim 10^{-9} \text{ Mpc}^{-3}$ (for the details, please see X. Fan et al. 2001). These observations suggest that massive black holes are not as prevalent as one might expect in the Universe's population of celestial objects.

In addition to the number density of massive black holes, other works constrain the proportion of black holes in the halo mass of galaxies. The constraints on the fraction of black holes in DM halos are more straightforward in limiting dark star formation, because the dark SFE in our work is described as a power-law model connected with the DM halo-mass function. Thus, we searched for possible constraints on the black hole fraction in the halo. Three constraints are suitable for this work because of the mass range and physical properties: (1) the constraint on black holes or compact DM with microlensing events near the cluster strong-lensing critical curves (M. Oguri et al. 2018); (2) the constraint from MACHO DM will dynamically heat the star cluster near the center of the ultrafaint dwarf galaxy (T. D. Brandt 2016); and (3) the constraints from the heat transfer between MACHOs and stars caused by gravitational scattering (P. W. Graham & H. Ramani 2024).

The Population III stars within the mass range of $140 \leq M_* \leq 260 M_\odot$ (A. Venditti et al. 2024) will not form

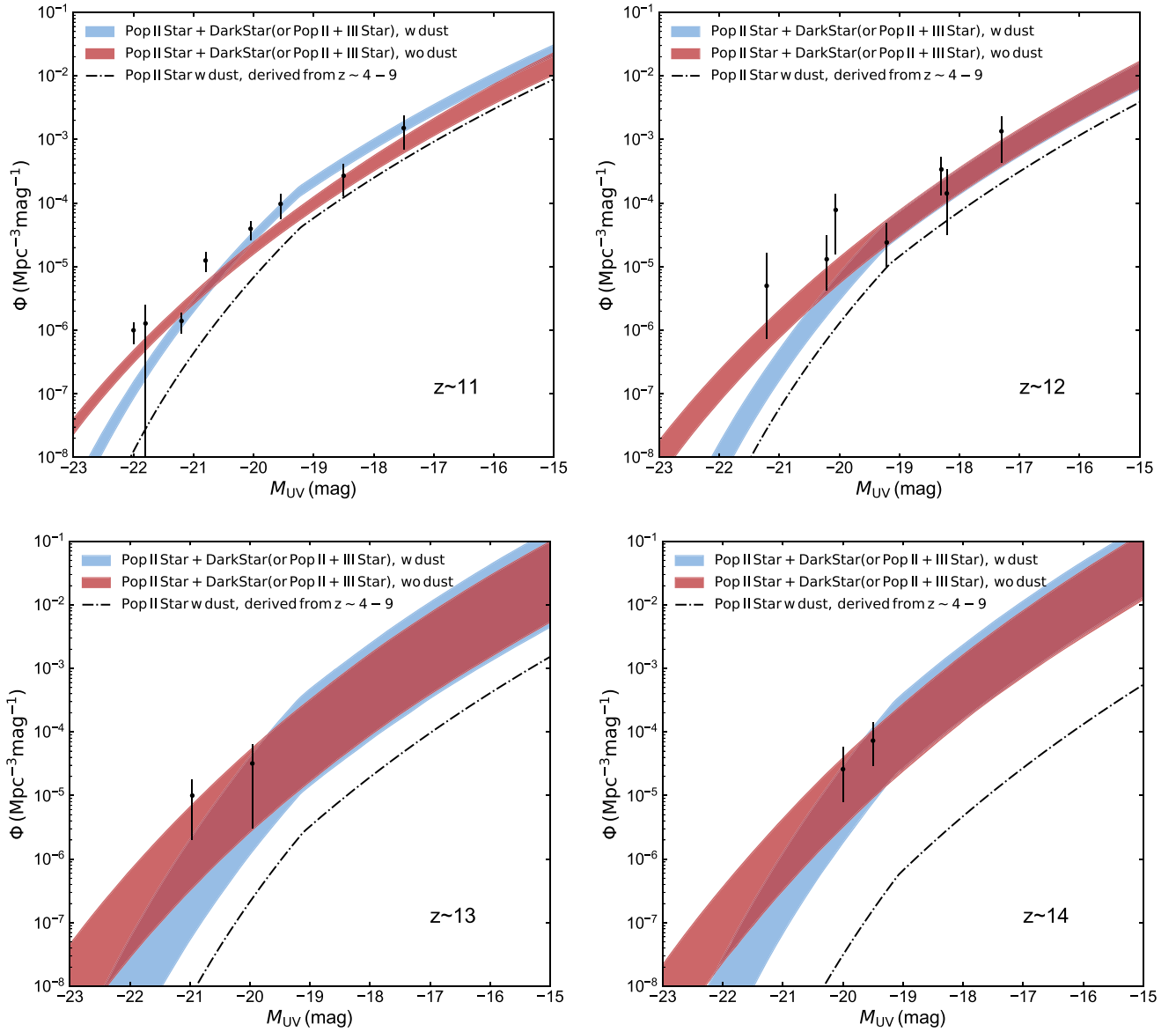


Figure 2. The UV LFs of galaxies at high redshift ($z > 10$), as observed by JWST, alongside model predictions. The UV LF data are compiled from diverse projects conducted with JWST (Y. Harikane et al. 2022b, 2023; R. Bouwens et al. 2023; R. J. Bouwens et al. 2023; C. T. Donnan et al. 2023; P. G. Pérez-González et al. 2023; C. M. Casey et al. 2024; D. J. McLeod et al. 2024). The 68.3% posterior regions of the Population II Star + Dark Star (or Population II + III Star) models, with and without dust, are represented by blue and red stripes, respectively. The black dashed–dotted line represents the predicted high-redshift Population II star model, which is derived from the extrapolation of low-redshift ($z \sim 4\text{--}9$) fitting results. The SFE models for both dark stars and Population II (Population III) stars are assumed to be identical.

black holes. Instead, they will experience the pair-instability supernova process, which leads to the ejection of most of their mass. However, dark stars with higher masses ($\geq 500 M_{\odot}$) will contribute to the population of MACHOs and provide minimal mass feedback to their surroundings.

After the deaths of those dark stars, the black holes formed can potentially be detected as sources of MACHOs. Those constraints derived from various experiments (T. D. Brandt 2016; M. Oguri et al. 2018; P. W. Graham & H. Ramani 2024) are depicted in Figure 3.

The transformation from the SFE and IMF to the halo fraction of black holes is estimated with the best-fitted effective SFEs of dark stars. The best-fitted effective SFEs of dark stars ($\epsilon_{\text{DS,eff}}$) correspond to the max likelihood curves in the effective halo-mass regions in Figure 4 (red or blue for cases with or without dust). The mass fraction of the relic black holes

can be estimated via (i.e., following B. Carr et al. 2021)

$$\psi(m) = \epsilon_{\text{DS,eff}} f_b \left(\frac{\xi_0 \phi(m) m^2}{M_{\text{tot}}} \right), \quad (11)$$

where M_{tot} is the total mass of the dark stars in Equation (A2).

The solid boxes in Figure 3 are the different halo fractions of the best-fitted SFEs of different mass ranges of IMFs ($500\text{--}10^4 M_{\odot}$ and $500\text{--}10^5 M_{\odot}$) in the $z \sim 14$ UV LF data set in cases without dust, corresponding to the deep red band in Figure 4. The orange dashed box is the mass fraction of the Population III stars within the mass range of $50\text{--}500 M_{\odot}$ that can explain the SFE excesses at $z > 10$. The dotted boxes are the allowed mass fractions of dark stars in the lower ranges of mass or SFE according to the constraints of MACHOs. The halo fractions of black holes from dark stars in conditions with

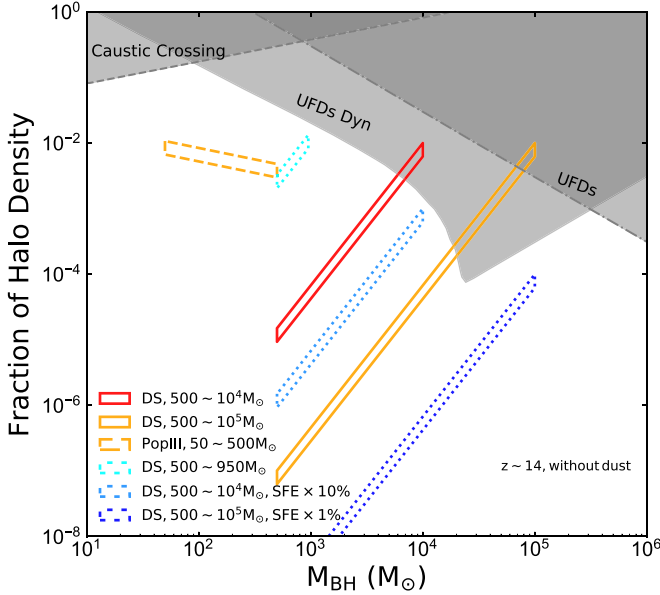


Figure 3. Constraints on the halo-mass fraction of dark stars. We adopt the results derived from various sources, including caustic crossings of strong-lensing arcs (M. Oguri et al. 2018), ultrafaint dwarf galaxies (UFDs; T. D. Brandt 2016), and dynamic heating of UFDs (P. W. Graham & H. Ramani 2024). The colorful boxes in solid lines represent the fraction results of the dark stars’ relic black holes of the best-fit SFEs of JWST UV LF $z \sim 14$ data, corresponding to the deep red band in Figure 4 of Appendix B. The orange dashed box is the mass fraction of the Population III stars model within the mass range of $50\text{--}500 M_{\odot}$. The dotted boxes are the allowed mass fractions of dark stars in the lower-mass range ($500\text{--}945 M_{\odot}$) or SFE ($\times 10\%$ within $500\text{--}10^4 M_{\odot}$ and $\times 1\%$ within $500\text{--}10^5 M_{\odot}$).

Table 2

The Best-fit Values and Posterior Results of the Dark Star (or Population III Star) SFE Parameters at $11 \leq z \leq 14$

z	Best Fit		Posterior ^a		$\ln(\mathcal{Z})$
	ϵ_{DS}	γ_{DS}	ϵ_{DS}	γ_{DS}	
With Dust					
11	0.076	0.520	$0.059^{+0.013}_{-0.017}$	$0.469^{+0.046}_{-0.075}$	79.76
12	0.005	0.004	$0.024^{+0.023}_{-0.017}$	$0.474^{+0.154}_{-0.188}$	58.75
13	0.179	0.335	$0.063^{+0.069}_{-0.045}$	$0.293^{+0.196}_{-0.150}$	34.84
14	0.201	0.296	$0.103^{+0.066}_{-0.060}$	$0.241^{+0.105}_{-0.120}$	18.49
Without Dust					
11	0.004	0.003	$0.012^{+0.011}_{-0.007}$	$0.452^{+0.221}_{-0.282}$	79.40
12	0.063	0.558	$0.025^{+0.024}_{-0.017}$	$0.469^{+0.145}_{-0.187}$	59.29
13	0.164	0.353	$0.066^{+0.058}_{-0.045}$	$0.309^{+0.162}_{-0.145}$	35.60
14	0.080	0.161	$0.090^{+0.064}_{-0.052}$	$0.249^{+0.107}_{-0.129}$	18.52

Note.

^a The listed errors of the posterior results are at the 68% credible level.

or without dust are similar, thus we show only the $z \sim 14$ result in the case without dust.

It is worth noting that the viability of a substantial fraction of very massive dark stars (i.e., $\geq 10^4 M_{\odot}$) may face challenges imposed by some constraints. As shown in the red and orange solid boxes in Figure 3, the relic black holes of dark stars with the top-heavy IMF have been excluded by the constraints of MACHOs. Due to the top-heavy IMF, the population of dark stars is dominated by supermassive members up to 10^4 or

$10^5 M_{\odot}$. Therefore, excluding the fraction of the massive part means the whole population is excluded by the constraints. To avoid the current constraints, the mass range of dark stars needs to be limited to $500\text{--}945 M_{\odot}$ (the dotted cyan box in Figure 3). The dotted sky blue (deep blue) box in the mass range $500\text{--}10^4 M_{\odot}$ ($500\text{--}10^5 M_{\odot}$) is the halo fraction of dark stars one-tenth (one-hundredth) lower than the halo fraction of the best-fitted SFE result. In that case, the SFE of the dark star needs to be much lower than the required values that can explain the JWST observations. However, the dark star mass is higher than $\sim 10^3 M_{\odot}$ from fitting the high-redshift-galaxy spectrum when the dark stars are considered as the primary UV radiation sources (see Figure 10); the details are described in Appendix C. Hence, the excess of SFE cannot be explained by the dark stars, because no appropriate mass range is allowed in the MACHO constraints and spectrum fitting.

Although the estimated mass ranges of dark stars derived from UV LFs have been nearly excluded, dark stars still have a slim chance of survival. When the formation efficiency of dark stars becomes lower, such constraints from MACHO become less effective. For example, in a $10^{10} M_{\odot}$ DM halo, the mass of the host galaxy is $10^8 M_{\odot}$ and the fraction of the halo density of a dark star with mass $\sim 10^5 M_{\odot}$ is $\sim 10^{-5}$, which is much lower than the current MACHO constraints. Therefore, the dark star can form in high-redshift galaxies indeed, but it is hard to explain the excess of SFE in JWST UV LF data.

In Section 2.2, we assumed that Population III stars and dark stars have the same SFE model but different IMFs. The Population III stars are expected to form in the dense region at high redshift. It may be possible to explain the excess of SFE without extra limitations from MACHOs. The solid boxes in Figure 3 illustrate the best-fitted fractions of Population III stars. However, given the current lack of clarity regarding the IMF and other specifics of Population III star formation, this analysis serves as a preliminary exploration of the data. For a more robust conclusion, future data and simulations are needed.

4. Discussion

In this study, we have evaluated the potential contribution of massive dark stars to the JWST UV LFs at extremely high redshifts. Our findings indicate that massive dark stars, with masses exceeding $1000 M_{\odot}$, which capture WIMPs as DM, could serve as a UV source in galaxies. This population could potentially account for the excess in SFE observed at redshifts $z \sim 11\text{--}14$. Nevertheless, current astrophysical constraints on the fraction of black holes within DM halos, derived from strong-lensing perturbations and galactic dynamics, impose stringent bounds on the formation efficiency of dark stars. Consequently, we propose that dark stars likely contribute a minor fraction to the observed SFE excesses.

Note that some interesting models have been proposed to account for the observed excesses in SFE. These include the roles of early dark energy (S. A. Adil et al. 2023; P. Wang et al. 2024) and dynamical dark energy (N. Menci et al. 2024), which might have influenced the expansion rate of the Universe and thus the formation of structures. Primordial black holes (B.-Y. Su et al. 2023; G.-W. Yuan et al. 2024) are other candidates that could contribute to the gravitational potential wells necessary for star formation. Furthermore, the nature of DM itself is a subject of ongoing debate (F. Nesti et al. 2023). Warm DM (H. Lin et al. 2024) and ultralight DM (Y. Gong et al. 2023; S. Bird et al. 2024) are alternatives to the cold DM

paradigm, potentially affecting the distribution and dynamics of matter in the early Universe. Cosmic strings (H. Jiao et al. 2023; Z. Wang et al. 2023), relics from phase transitions in the early Universe, could also play a role in structure formation. In addition to these, other mechanisms such as feedback-free processes (A. Dekel et al. 2023; Z. Li et al. 2024) and Population III star formation (K. Inayoshi et al. 2022; L. Y. A. Yung et al. 2024) should be considered. These mechanisms could provide alternative explanations for the high-redshift SFE excesses and should be distinguished from the new physics mentioned above in future studies.

Acknowledgments

We thank the reviewers for their helpful comments. We thank Steven Finkelstein, Qiao Li, Yong-Jia Huang, Tian-Peng Tang, Yue-Lin Sming Tsai, Hao-Jing Yan, Hai-Bo Yu, Qiang Yuan, Chi Zhang, Tian-Ci Zheng, and Hao Zhou for their helpful discussions. This work is supported by the National Key Research and Development Program of China (No. 2022YFF0503304), the Natural Science Foundation of China (No. 11921003), the China Postdoctoral Science Foundation (No. 2023TQ0355), and the New Cornerstone Science Foundation through the XPLORER PRIZE. G.-W.Y. also acknowledges support from the University of Trento and the Provincia Autonoma di Trento through the UniTrento Internal Call for Research 2023 grant ‘‘Searching for Dark Energy off the beaten track’’ (DARKTRACK, grant agreement No. E63C22000500003, PI: Sunny Vagnozzi).

Software: astropy (Astropy Collaboration et al. 2013, 2018, 2022), CAMB (A. Lewis et al. 2000), pymultinest (J. Buchner et al. 2014), matplotlib (J. D. Hunter 2007), numpy (C. R. Harris et al. 2020), scipy (P. Virtanen et al. 2020), bagpipes (A. C. Carnall et al. 2018, 2019).

Appendix A

UV-luminosity-to-SFR Conversion Factor \mathcal{K}_{UV}

The \mathcal{K}_{UV} can be calculated by two methods: spectrum integrations or the mass-to-luminosity ratio (M/L). Previously, Y. Harikane et al. (2023) used spectral synthesis code to search for Population III stars in the first galaxies. The M/L is also used to roughly estimate the luminosity arising from the IMFs in galaxies (A. Venditti et al. 2024).

To compare the dark stars and Population III stars at high redshifts, we calculate the M/L of dark stars and Population III

stars to derive the UV-luminosity-to-SFR conversion factor:

$$M/L = \frac{M_{\text{tot}}}{L_{\text{tot}}}. \quad (\text{A1})$$

The total mass of a given IMF is

$$M_{\text{tot}} = \int_{m_{\text{low}}}^{m_{\text{up}}} \xi_0 m \phi(m) dm, \quad (\text{A2})$$

where m_{up} is the upper truncation of stellar mass, m_{low} is the lower truncation of stellar mass, ξ_0 is a consistency, and $\phi(m)$ is the IMF. The Salpeter IMF and top-heavy IMF are of the same type $\phi(m) \propto m^{-\alpha}$ with a different slope α . The index is $\alpha = 2.35$ for the Salpeter IMF and is $\alpha = -0.17$ for the top-heavy IMF used in A. Venditti et al. (2024). In this work, we use a top-heavy IMF with $\alpha = -0.17$ for calculating the M/L of the dark stars. The IMF slope $\alpha = 2.35$ is used for Population III stars, which corresponds to a conversion factor $\mathcal{K}_{UV} = 2.80 \times 10^{-29} M_{\odot} \text{ yr}^{-1} / (\text{erg s}^{-1} \text{ Hz}^{-1})$ used in K. Inayoshi et al. (2022) and Y. Y. Wang et al. (2023).

For the Population III stars and dark stars with $m \geq 50 M_{\odot}$, the total luminosity of the population with a given IMF is

$$L_{\text{tot}} = \int_{m_{\text{low}}}^{m_{\text{up}}} \xi_0 L(m) \phi(m) dm, \quad (\text{A3})$$

where $L(m)$ is the standard mass-to-luminosity relation of Population III stars or dark stars.

For dark stars and Population III stars, $L(m)$ is derived from the interpolation of the Hertzsprung–Russell (H-R) diagrams in K. Freese et al. (2010) and R. S. Klessen & S. C. O. Glover (2023), respectively.

With the above equations, we can calculate the \mathcal{K}_{UV} of the dark stars:

$$\frac{\mathcal{K}_{UV,DS}}{\mathcal{K}_{UV,Pop III}} = \frac{(M/L)_{DS}}{(M/L)_{Pop III}}. \quad (\text{A4})$$

Table 3 shows the UV-luminosity-to-SFR conversion factor \mathcal{K}_{UV} of stars, Population III stars, and dark stars. The values of Population II/I stars and Population III stars are taken from K. Inayoshi et al. (2022). For dark stars, we calculated the values of two IMFs with the above method. Following K. Inayoshi et al. (2022), we also gave the values of η_{UV} and $\epsilon_{*,\text{rad}}$ in Table 3. K. Inayoshi et al. (2022) defined the η_{UV} as $\eta_{UV} = \frac{L_{UV,\nu_0}}{\text{SFR}}$, where $\nu_0 \simeq 8.3 \text{ eV}$ corresponds to the characteristic UV wavelength $\lambda_0 = 1500 \text{ \AA}$. The $\epsilon_{*,\text{rad}} = \frac{L_{UV}}{\text{SFR} \cdot c^2}$ is defined as the UV radiative efficiency of star formation for a given SFR by K. Inayoshi et al. (2022).

Table 3
UV-luminosity-to-SFR Conversion Factor of Stars, Population III Stars, and Dark Stars

Population Type	IMF Type	m_{low} (M_{\odot})	m_{up} (M_{\odot})	α	Z (Z_{\odot})	$\mathcal{K}_{\text{UV}}^{\text{a}}$ $\frac{M_{\odot} \text{ yr}^{-1}}{(\text{erg s}^{-1} \text{ Hz}^{-1})}$	$\eta_{\text{UV}}^{\text{a}}$ $\frac{\text{erg s}^{-1} \text{ Hz}^{-1}}{(M_{\odot} \text{ yr}^{-1})}$	$\epsilon_{*,\text{rad}}^{\text{b}}$
Stars ^c	Salpeter	1×10^{-1}	1×10^2	2.35	0.02	1.26×10^{-28}	7.94×10^{27}	2.79×10^{-4}
Stars ^c	Salpeter	1×10^{-1}	1×10^2	2.35	0.0004	1.07×10^{-28}	9.32×10^{27}	3.28×10^{-4}
Population III ^c	Salpeter	5×10^1	5×10^2	2.35	0	2.80×10^{-29}	3.57×10^{28}	1.26×10^{-3}
DS, w Cap $m_{\chi} = 10 \text{ Gev}$	Power law	5×10^2	1×10^5	-0.17	0	2.79×10^{-29}	3.59×10^{28}	1.27×10^{-3}
DS, w Cap $m_{\chi} = 100 \text{ Gev}$	Power law	5×10^2	1×10^5	-0.17	0	2.59×10^{-29}	3.86×10^{28}	1.36×10^{-3}
DS, w Cap $m_{\chi} = 1 \text{ Tev}$	Power law	5×10^2	1×10^5	-0.17	0	2.70×10^{-29}	3.70×10^{28}	1.31×10^{-3}
DS, w Cap $m_{\chi} = 10 \text{ Gev}$	Power law	5×10^2	1×10^4	-0.17	0	3.88×10^{-29}	2.58×10^{28}	9.10×10^{-4}
DS, w Cap $m_{\chi} = 100 \text{ Gev}$	Power law	5×10^2	1×10^4	-0.17	0	3.59×10^{-29}	2.78×10^{28}	9.82×10^{-4}
DS, w Cap $m_{\chi} = 1 \text{ Tev}$	Power law	5×10^2	1×10^4	-0.17	0	3.30×10^{-29}	3.03×10^{28}	1.70×10^{-3}
DS, wo Cap $m_{\chi} = 10 \text{ Gev}$	Power law	5×10^2	1×10^5	-0.17	0	2.28×10^{-29}	4.38×10^{28}	1.55×10^{-3}
DS, wo Cap $m_{\chi} = 100 \text{ Gev}$	Power law	5×10^2	1×10^5	-0.17	0	2.58×10^{-29}	3.88×10^{28}	1.37×10^{-3}
DS, wo Cap $m_{\chi} = 1 \text{ Tev}$	Power law	5×10^2	1×10^5	-0.17	0	2.76×10^{-29}	3.62×10^{28}	1.28×10^{-3}
DS, wo Cap $m_{\chi} = 10 \text{ Gev}$	Power law	5×10^2	1×10^4	-0.17	0	1.63×10^{-29}	6.14×10^{28}	2.17×10^{-3}
DS, wo Cap $m_{\chi} = 100 \text{ Gev}$	Power law	5×10^2	1×10^4	-0.17	0	2.87×10^{-29}	3.48×10^{28}	1.23×10^{-3}
DS, wo Cap $m_{\chi} = 1 \text{ Tev}$	Power law	5×10^2	1×10^4	-0.17	0	3.12×10^{-29}	3.21×10^{28}	1.13×10^{-3}

Notes.

^a K. Inayoshi et al. (2022) defined the η_{UV} as $\eta_{\text{UV}} = \frac{L_{\text{UV},\nu_0}}{\text{SFR}}$, where $\nu_0 \simeq 8.3 \text{ eV}$ corresponds to the characteristic UV wavelength $\lambda_0 = 1500 \text{ \AA}$.

^b The $\epsilon_{*,\text{rad}} = \frac{L_{\text{UV}}}{\text{SFR} \cdot v^2}$ is defined as the UV radiative efficiency of star formation for a given SFR by K. Inayoshi et al. (2022).

^c The values are taken from K. Inayoshi et al. (2022).

The result for \mathcal{K}_{UV} shows a similar UV emission capability in different WIMP DM masses or upper limits of dark star masses, which is in a range of 0.7–1.7 times compared with the Population III stars. It shows similar properties of dark stars and Population III stars in the high-redshift galaxies.

The \mathcal{K}_{UV} values of the dark stars are similar to those of Population III stars, which are lower than Population II/I stars. Meanwhile, the UV emission efficiency $\epsilon_{*,\text{rad}}$ of the dark stars is similar to that of Population III stars, which is higher than Population II/I stars. That indicates a lower SFE in fitting the UV LFs with a \mathcal{K}_{UV} of the dark stars or Population III stars compared with Population II/I stars at lower redshift.

Appendix B SFE Result of UV LF Fitting

At the redshift range from 4 to 9, the profiles of Population II SFEs are assumed to be uniform and independent of redshift increasing. As shown in Figure 1, the SFE is constrained in a tight range and the UV LFs are fitted well. At higher redshifts,

$z > 10$, the contribution of the Population II stars' component to the total SFE follows the results in Figure 1. Therefore, the dark stars (or Population III stars) contribute the extra component of the total SFE.

Figure 4 shows the best-fit SFE models in different redshift bins with dark stars (or Population III stars) with dust attenuation and without dust attenuation. The blue or red dashed lines show the 68% SFE of Population II stars in a range of $z \sim 4\text{--}9$ with or without dust, respectively. The colored region of the solid line shows the best-fit 68% SFE model of dark stars (or Population III stars). Our result indicates that the presence of dark stars (or Population III stars) could reduce the high rate of star formation required for JWST galaxy observations, which is consistent with the current efficiency ($\sim 16\%$).

We also plot the corners of the posteriors in Figures 5 and 6. The dark red regions of the three depths in the corner plots of Figures 5 and 6 represent 68%, 95%, and 99% confidence intervals, respectively. The black crosses are the positions of the best-fit parameters.

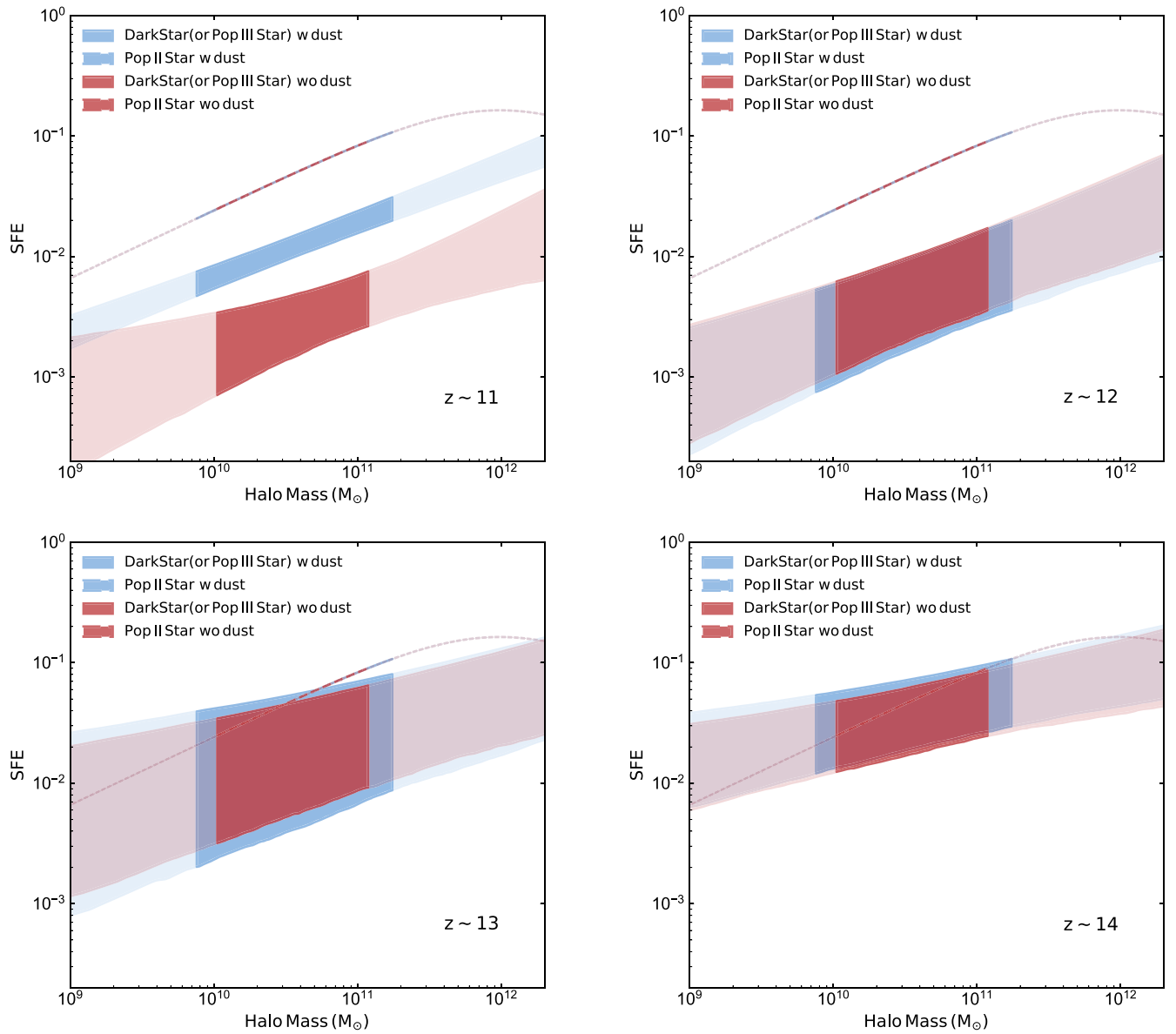


Figure 4. Best-fit SFE models in different redshift bins with dark stars (or Population III stars), with and without dust attenuation. The blue or red dashed lines show the 68% SFE of Population II stars in a range of $z \sim 4-9$ with or without dust, respectively. The blue or red regions show the 68% best-fit SFE model of dark stars with or without dust.

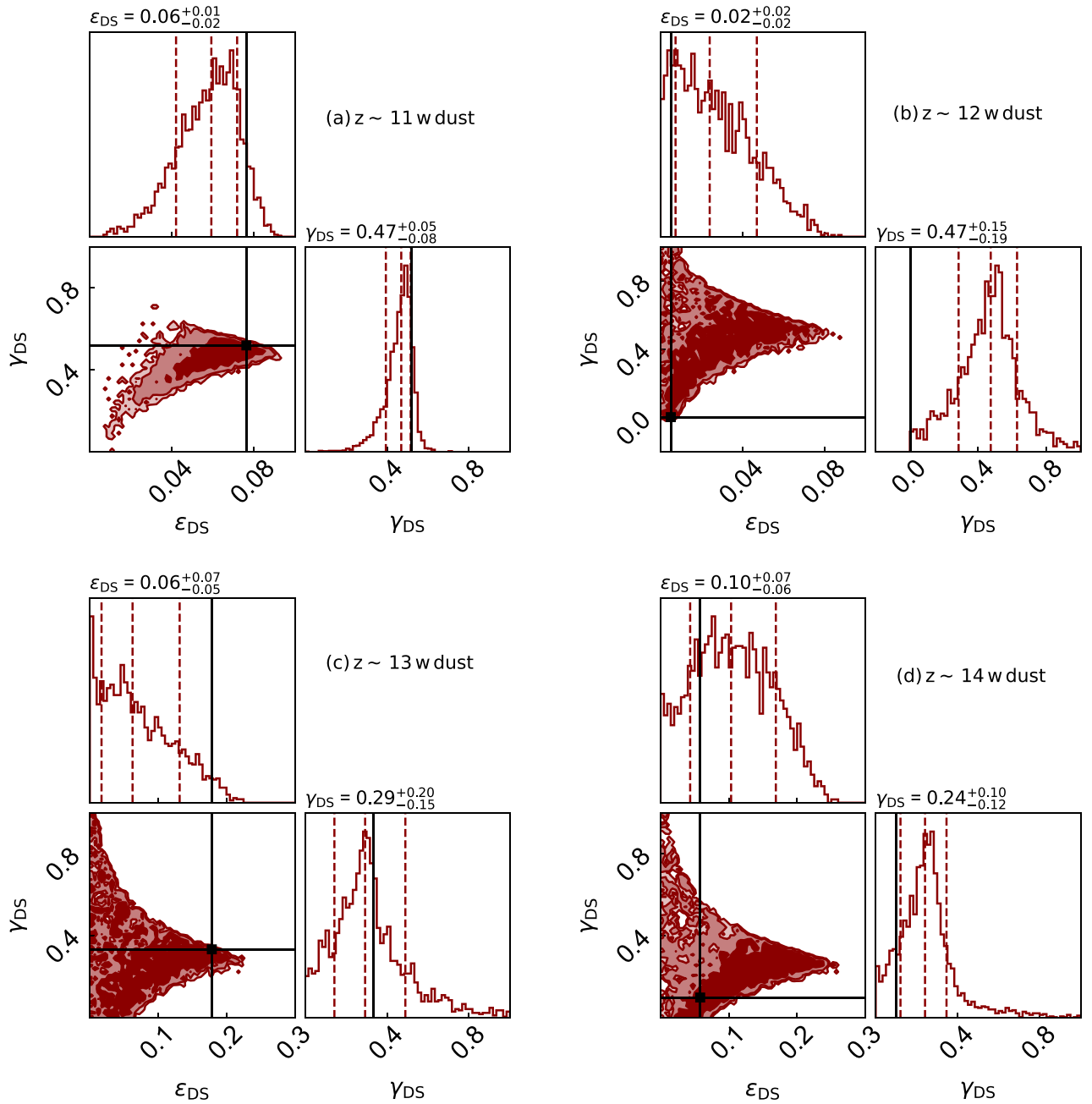


Figure 5. The posteriors of dark star or Population III star SFE models considering dust attenuation. The dark red regions of the three depths in the corner plots are labeled with 68%, 95%, and 99% confidence intervals, respectively. The black crosses are the positions of the best-fit parameters.

Appendix C

Constraint on Dark Star Properties with JWST Spectrum

The properties of dark stars can be effectively constrained through the fitting of spectra obtained from high-redshift galaxies at $z > 12$. At such high redshift, the galaxy spectrum may be dominated by massive dark stars when the stellar populations within the galaxy consist of a mixture of traditional stars and dark stars. By analyzing the spectrum of high-redshift galaxies, it becomes possible to constrain both the DM mass and the dark stars. In this context, we perform a fitting procedure for the dark star temperature, assuming that the UV radiation is primarily governed by the presence of massive dark stars.

As a pertinent example, JADES-GS-z13-0 stands out as a spectrum-confirmed galaxy positioned at a redshift of $z = 13.2$,

characterized as a metal-poor young galaxy (E. Curtis-Lake et al. 2023). Its NIRSpec data have been made publicly available in M. Rieke et al. (2023) and A. J. Bunker et al. (2024) and the data reduction processes can be found in D. J. Eisenstein et al. (2023) and F. D’Eugenio et al. (2024). We leverage this galaxy spectrum to fit the parameters associated with dark stars and WIMPs. This data set provides a valuable opportunity to refine our understanding of the physical characteristics of dark stars and their interplay with WIMPs in the high-redshift galaxy environment.

We rescale the dark stars’ blackbody spectral model (BB_{DS}) with varying temperatures and the young stellar spectra from Bagpipes to achieve a matching flux of $\text{flux}_{1500 \text{ \AA}} = 6.56 \times 10^{21} \text{ erg s}^{-1} \text{ cm}^{-2} \text{ \AA}^{-1}$ for the galaxy JADES-GS-

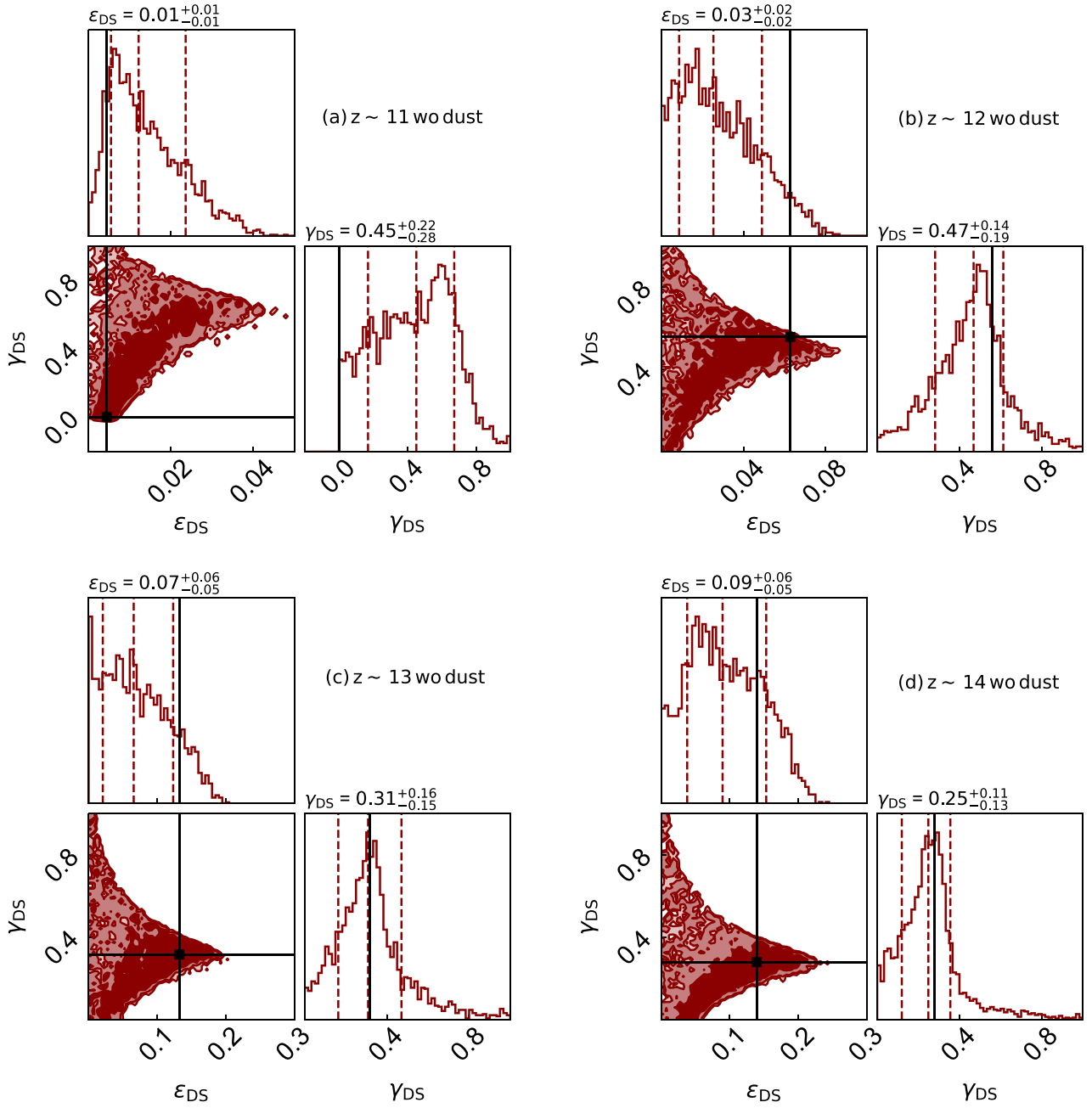


Figure 6. The posteriors of dark star or Population III star SFE models without considering dust attenuation. The dark red regions of the three depths in the corner plots are labeled with 68%, 95%, and 99% confidence intervals, respectively. The black crosses are the positions of the best-fit parameters.

z_{13-0} spectrum at 1500 \AA . The flux at 1500 \AA is calculated using a $\sim 200 \text{ \AA}$ top-hat filter, represented by the purple band in Figure 7. Subsequently, we performed a fitting procedure to determine the temperature T of $\text{BB}_{\text{DS}}(T)$ and the fraction of dark star UV radiation at 1500 \AA (R_{DS}). The priors of R_{DS} and $\log(T)$ are uniform distributions within the specified ranges.

With the fitting results of the JWST UV LFs of $z > 10$ galaxies, we derive the range of prior fractions for the UV radiation of dark stars at 1500 \AA (R_{DS}):

$$R_{\text{DS}, M_h} \equiv \frac{f_{\text{DS}, M_h} \mathcal{K}_{\text{UV}, S}}{f_{\text{DS}, M_h} \mathcal{K}_{\text{UV}, S} + f_{S, M_h} \mathcal{K}_{\text{UV}, \text{DS}}}, \quad (\text{C5})$$

where f_{DS, M_h} is the SFE of the dark stars at a halo mass M_h in Equation (6), $\mathcal{K}_{\text{UV}, S}$ is the UV-luminosity-to-SFR conversion factor of stars, and $\mathcal{K}_{\text{UV}, \text{DS}}$ is the UV-luminosity-to-SFR conversion factor of dark stars. For the redshift bin $z \sim 13$, we set the prior of R_{DS} as $\sim 0\% - 84.5\%$.

We use the galaxy spectrum Bayesian analysis tool Bagpipes (A. C. Carnall et al. 2018, 2019) to construct the spectrum of a galaxy with young stellar populations. For modeling the dark star spectrum, we use a blackbody model (BB_{DS}). To specify the properties of the young stellar component, we assign an age of approximately $\sim 200 \text{ Myr}$, corresponding to the onset of star formation at a redshift of $z \sim 25$. The metallicity of

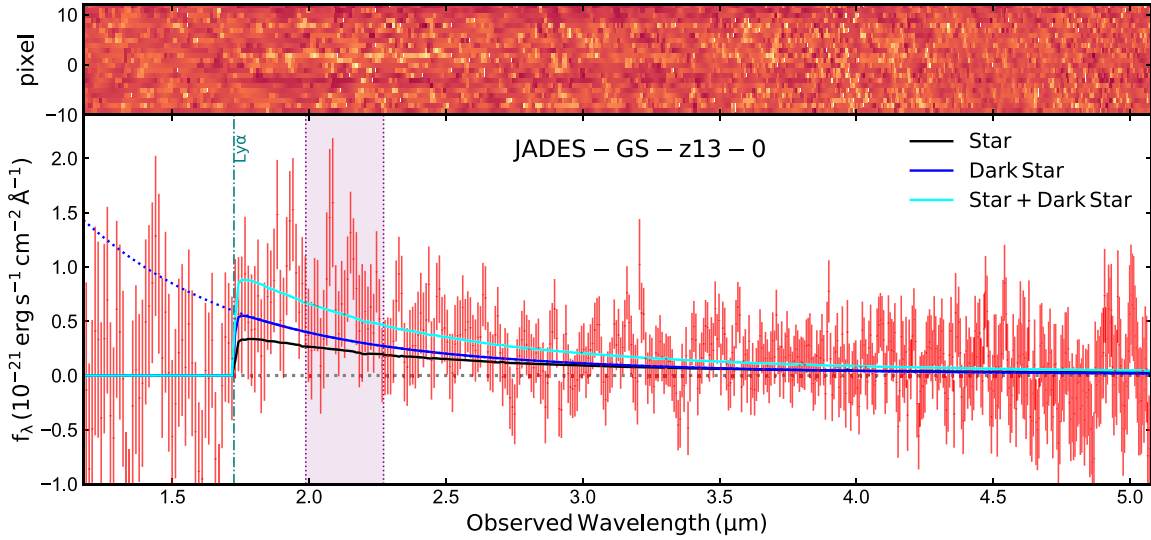


Figure 7. The JWST/NIRSpec spectrum and best-fit spectrum model of JADES-GS-z13-0. The yellow solid line shows the young-stellar-component contributions to the galaxy model from the software Bagpipes (A. C. Carnall et al. 2018, 2019). The solid or dotted blue lines are the absorbed or unabsorbed blackbody models of dark stars, respectively. The cyan solid line is the best-fit total spectrum model in this work. The red error bars are the NIRSpec spectrum of the galaxy. The NIRSpec data have been released in A. J. Bunker et al. (2024). The purple band is a filter window at 1500 Å with width 200 Å.

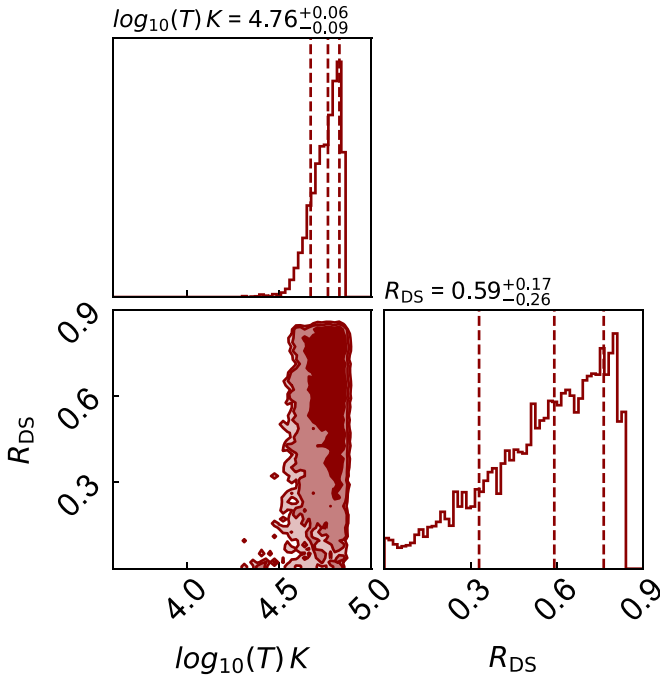


Figure 8. The posteriors of fitting the galaxy spectrum of JADES-GS-z13-0.

the young stellar populations is set as $\log(Z/Z_{\odot}) = -1.69$ (E. Curtis-Lake et al. 2023). The nebular ionization emission is determined by the ionization parameter $\log U$; following E. Curtis-Lake et al. (2023), we estimate it with metallicity:

$$\log U_s = -3.638 + 0.055Z + 0.68Z^2. \quad (\text{C6})$$

The total flux of the galaxy at wavelength λ_i is given by the equation

$$\text{flux}_{\text{tot}, \lambda_i} = R_{\text{DS}} \text{flux}_{\text{BB}_{\text{DS}}(T), \lambda_i} + (1 - R_{\text{DS}}) \text{flux}_{\text{YS}, \lambda_i}. \quad (\text{C7})$$

Although dark stars can emit UV photons with higher energy than 13.4 eV, the far-UV radiation will be absorbed by the neutral intergalactic medium (IGM). Thus, we calculate an accurate profile of the damping wing of the Gunn–Peterson trough caused by a homogeneous neutral IGM. Following J. Miralda-Escudé (1998), the optical depth of the Ly α damping-wing absorption is described by an exponential index $\tau(\Delta\lambda)$:

$$\tau(\Delta\lambda) = \frac{\tau_0 R_{\alpha}}{\pi} (1 + \delta)^{3/2} \int_{x_1}^{x_2} \frac{dx x^{9/2}}{(1-x)^2}, \quad (\text{C8})$$

where $\delta \simeq \Delta\lambda/[\lambda_{\alpha}(1+z_s)]$, $x_1 = (1+z_n)/[(1+z_s)(1+\delta)]$, $z_s = 13.20$ is the source redshift, $z_n = 13.17$ is the redshift of the foreground neutral IGM that is constrained by E. Curtis-Lake et al. (2023), $x_2 = (1+\delta)^{-1}$, and the integral is given by J. Miralda-Escudé (1998):

$$\int_{x_1}^{x_2} \frac{dx x^{9/2}}{(1-x)^2} = \frac{x_2^9}{1-x_2} + \frac{9}{7}x_2^7 + \frac{9}{5}x_2^5 + 3x_2^3 + 9x_2 - \frac{9}{2} \log \frac{1+x_2^2}{1-x_2^2}. \quad (\text{C9})$$

Hence, the total flux of the galaxy spectrum model is

$$\text{Flux}_{\text{tot}, \lambda_i} = e^{-\tau(\Delta\lambda)} \text{flux}_{\text{tot}, \lambda_i}. \quad (\text{C10})$$

In the fitting procedure, we first fitted the dark star parameters R_{DS} and T . After correcting the IGM absorption with Equation (C10), the total best-fitted flux needs a total shift into a more well-fitted case, because the above scaling of the blackbody and young stellar spectra is limited in a ~ 200 Å top-hat filter. We then used a total flux amplitude to fit the best-fitted spectrum model including $\text{BB}_{\text{DS}}(T)$ and young stellar spectra. The best-fit amplitude of the total spectral model is 0.65 ± 0.04 at the 1σ confidence level.

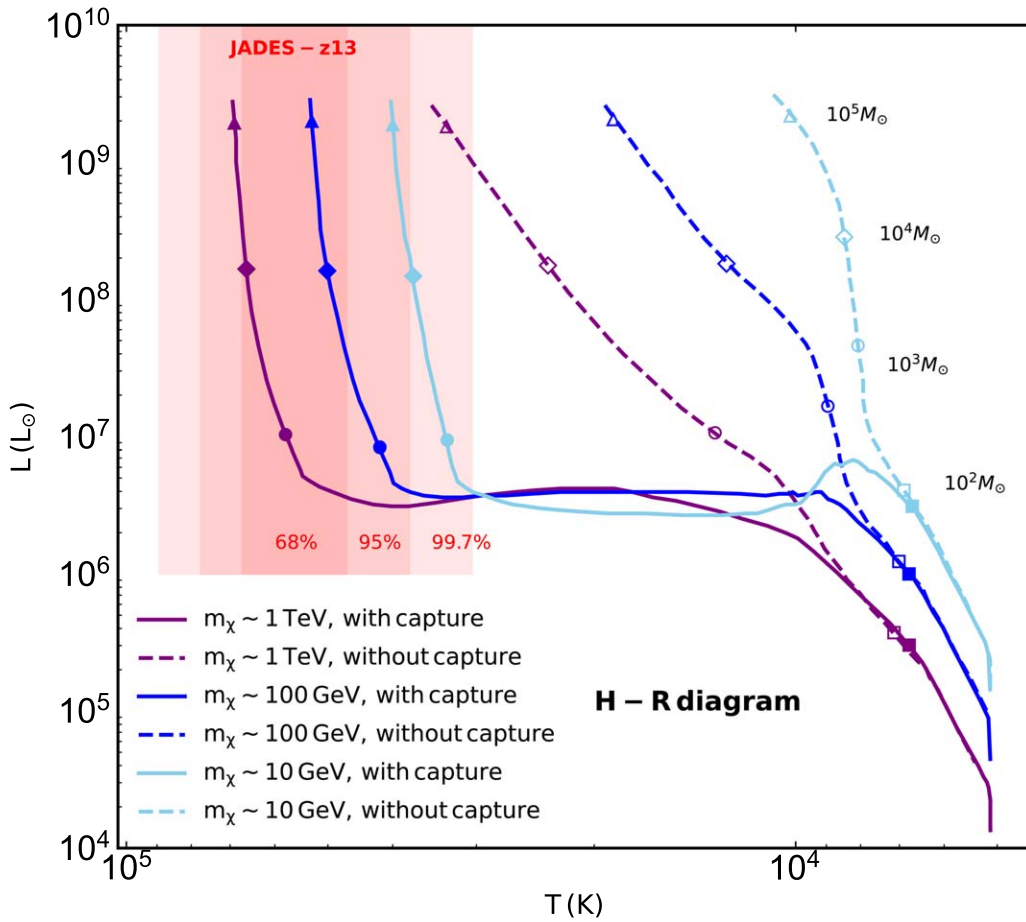


Figure 9. H-R diagram of dark stars and the posteriors of the dark stars’ temperature with JWST spectrum of JADES-z13. The H-R diagram is reproduced from K. Freese et al. (2010). The red regions with different depths are the 68%, 95%, and 99.7% posterior regions of the dark star temperature, by fitting the spectrum of the object JADES-z13.

In Figure 7, we present the JWST/NIRSpec spectrum and its best-fit model parameters, with the posteriors of the two parameters R_{DS} and T being shown in Figure 8. Furthermore, we display the H-R diagram of dark stars and the posteriors of the dark stars’ temperature with the JWST spectrum of JADES-z13 in Figure 9.

In Figure 7, the best-fit model and the JWST/NIRSpec spectrum are presented, revealing the dominance of the dark star in the galaxy spectrum, with the stellar component contributing secondarily in the UV band. Figure 8 displays the posteriors of the two parameters R_{DS} and T , indicating a blackbody temperature of the dark stars’ surface in the galaxy at $\sim 5.75 \times 10^4$ K. Furthermore, the estimated fraction of UV radiation contributed by the dark stars in the galaxy is approximately 59%.

Appendix D The Properties of WIMP DM

The properties of dark stars are intricately linked to the particle mass of WIMPs. In the study conducted by K. Freese et al. (2010), dark stars’ physical characteristics are explored under two scenarios: one “with capture” and the other “without

capture.” To visualize the distribution of dark stars in the H-R diagram, we present Figure 9. The dark stars, with varying masses, exhibit distinct temperatures and luminosities on the H-R diagram. Leveraging this diagram, we constrain the parameters of the WIMP DM and the mass of the dark stars. The results, particularly for the “with capture” scenario, are displayed in Figure 10. Notably, our finding underscores the necessity of very massive dark stars, exceeding $\sim 10^3 M_{\odot}$, due to the strong suppression of the luminosity at lower masses (see also Figure 9 in Appendix C). Conversely, in the case of “without capture,” no suitable parameter region was identified.

Our results presented in Figure 10 indicate a preference for WIMPs with masses ranging from tens of gigaelectronvolts to a few teraelectronvolts. Intriguingly, this range aligns with the gigaelectronvolt gamma-ray excess observed in the inner Galaxy (D. Hooper & L. Goodenough 2011; B. Zhou et al. 2015), the possible antiproton excess (M. Y. Cui et al. 2017), and the W-boson mass anomaly (CDF Collaboration et al. 2022). The consistent interpretation of these phenomena as the annihilation of ~ 50 – 70 GeV WIMPs (Y. Z. Fan et al. 2022; C. R. Zhu et al. 2022) adds support to the hypothesis that the annihilation of WIMPs can fuel the dark stars discussed in this study.

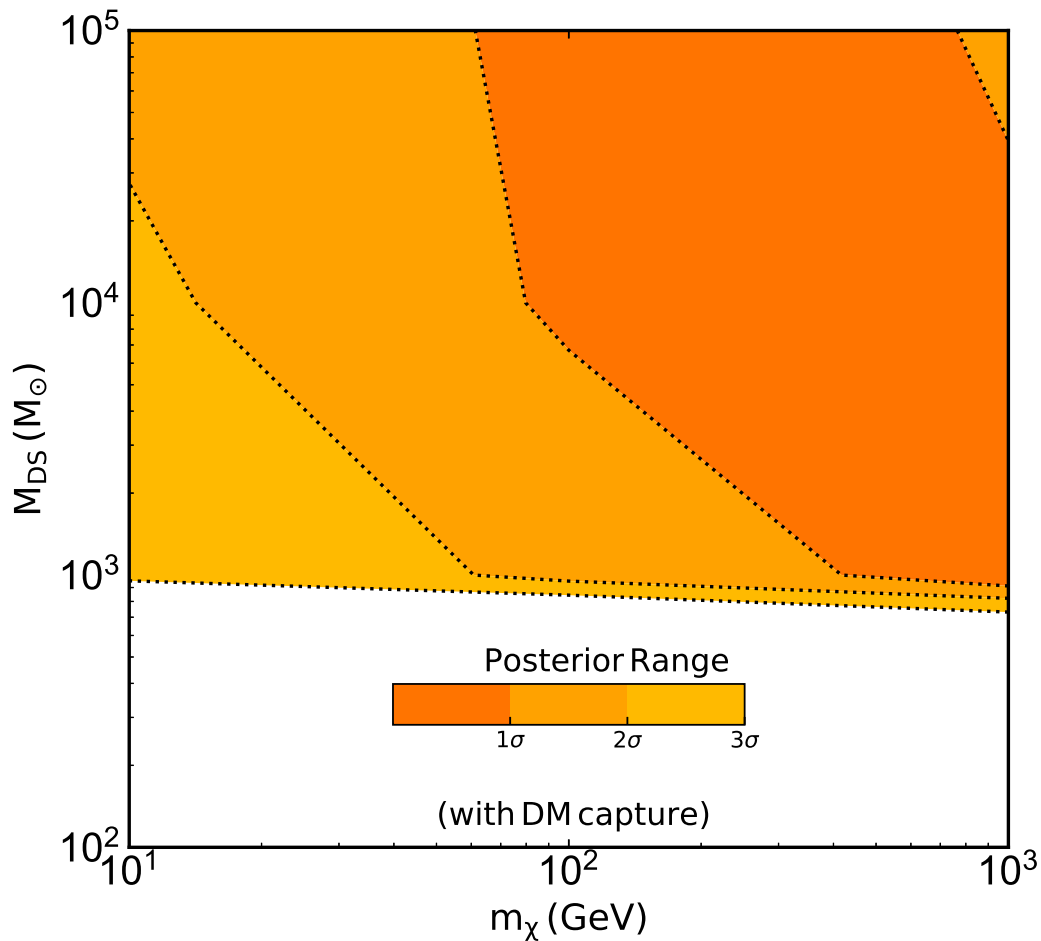


Figure 10. The posterior distribution of the dark stars' parameter M_{DS} and the mass parameter m_χ for WIMPs.

ORCID iDs

Lei Lei (雷磊) <https://orcid.org/0000-0003-4631-1915>
 Yi-Ying Wang (王艺颖) <https://orcid.org/0000-0003-1215-6443>
 Guan-Wen Yuan (袁官文) <https://orcid.org/0000-0002-4538-8526>
 Tong-Lin Wang (王彤琳) <https://orcid.org/0009-0004-0029-6080>
 Martin A. T. Groenewegen <https://orcid.org/0000-0003-2723-6075>
 Yi-Zhong Fan (范一中) <https://orcid.org/0000-0002-8966-6911>

References

- Adams, N. J., Conselice, C. J., Austin, D., et al. 2024, *ApJ*, **965**, 169
 Adil, S. A., Mukhopadhyay, U., Sen, A. A., & Vagnozzi, S. 2023, *JCAP*, 2023, 072
 Astropy Collaboration, Price-Whelan, A. M., Lim, P. L., et al. 2022, *ApJ*, **935**, A167
 Astropy Collaboration, Price-Whelan, A. M., Sipőcz, B. M., et al. 2018, *AJ*, **156**, 123
 Astropy Collaboration, Robitaille, T. P., Tollerud, E. J., et al. 2013, *A&A*, **558**, A33
 Behroozi, P. S., & Silk, J. 2015, *ApJ*, **799**, 32
 Bird, S., Chang, C.-F., Cui, Y., & Yang, D. 2024, *PhLB*, 858, 139062
 Bouwens, R., Illingworth, G., Oesch, P., et al. 2023, *MNRAS*, **523**, 1009
 Bouwens, R. J., Oesch, P. A., Stefanon, M., et al. 2021, *AJ*, **162**, 47
 Bouwens, R. J., Stefanon, M., Brammer, G., et al. 2023, *MNRAS*, **523**, 1036
 Bowler, R. A. A., Jarvis, M. J., Dunlop, J. S., et al. 2020, *MNRAS*, **493**, 2059
 Boylan-Kolchin, M. 2023, *NatAs*, **7**, 731
 Brandt, T. D. 2016, *ApJL*, **824**, L31
 Buchner, J., Georgakakis, A., Nandra, K., et al. 2014, *A&A*, **564**, A125
 Bunker, A. J., Cameron, A. J., Curtis-Lake, E., et al. 2024, *A&A*, **690**, A288
 Carnall, A. C., McLure, R. J., Dunlop, J. S., & Davé, R. 2018, *MNRAS*, **480**, 4379
 Carnall, A. C., McLure, R. J., Dunlop, J. S., et al. 2019, *MNRAS*, **490**, 417
 Carr, B., Kohri, K., Sendouda, Y., & Yokoyama, J. 2021, *RPPh*, **84**, 116902
 Casey, C. M., Akins, H. B., Shuntov, M., et al. 2024, *ApJ*, **965**, 98
 CDF Collaboration, Amerio, T., Amidei, S., et al. 2022, *Sci*, **376**, 170
 Colgáin, E. Ó, Sheikh-Jabbari, M. M., & Yin, Lu 2024, arXiv:2405.19953
 Cui, M.-Y., Yuan, Q., Tsai, Y.-L. S., & Fan, Y.-Z. 2017, *PRL*, **118**, 191101
 Curtis-Lake, E., Carniani, S., Cameron, A., et al. 2023, *NatAs*, **7**, 622
 Dekel, A., Sarkar, K. C., Bimboim, Y., Mandelker, N., & Li, Z. 2023, *MNRAS*, **523**, 3201
 D'Eugenio, F., Cameron, A. J., Scholtz, J., et al. 2024, arXiv:2404.06531
 Donnan, C. T., McLeod, D. J., Dunlop, J. S., et al. 2023, *MNRAS*, **518**, 6011
 Eisenstein, D. J., Willott, C., Alberts, S., et al. 2023, arXiv:2306.02465
 Fan, X., Narayanan, V. K., Lupton, R. H., et al. 2001, *AJ*, **122**, 2833
 Fan, Y. Z., Tang, T.-P., Tsai, Y.-L. S., & Wu, L. 2022, *PhRvL*, **129**, 091802
 Feroz, F., Hobson, M. P., & Bridges, M. 2009, *MNRAS*, **398**, 1601
 Finkelstein, S. L., Bagley, M. B., Ferguson, H. C., et al. 2023, *ApJL*, **946**, L13
 Finkelstein, S. L., Leung, G. C. K., Bagley, M. B., et al. 2024, *ApJL*, **969**, L2
 Freese, K., Gondolo, P., & Spolyar, D. 2008, in AIP Conf. Ser. 990, First Stars III, ed. B. W. O'Shea & A. Heger (Melville, NY: AIP), 42
 Freese, K., Ilie, C., Spolyar, D., Valluri, M., & Bodenheimer, P. 2010, *ApJ*, **716**, 1397
 Freese, K., Rindler-Daller, T., Spolyar, D., & Valluri, M. 2016, *RPPh*, **79**, 066902
 Glover, S. 2013, in Astrophysics and Space Science Library, Vol. 396, The First Galaxies, ed. T. Wiklind, B. Mobasher, & V. Bromm (Berlin: Springer), 103
 Gondolo, P., Sandick, P., Shams Es Haghi, B., & Visbal, E. 2022, *ApJ*, **935**, 11
 Gong, Y., Yue, B., Cao, Y., & Chen, X. 2023, *ApJ*, **947**, 28

- Graham, P. W., & Ramani, H. 2024, *PhRvD*, **110**, 075011
- Greene, J. E., Strader, J., & Ho, L. C. 2020, *ARA&A*, **58**, 257
- Harikane, Y., Inoue, A. K., Mawatari, K., et al. 2022b, *ApJ*, **929**, 1
- Harikane, Y., Nakajima, K., Ouchi, M., et al. 2024, *ApJ*, **960**, 56
- Harikane, Y., Ono, Y., Ouchi, M., et al. 2022a, *ApJS*, **259**, 20
- Harikane, Y., Ouchi, M., Oguri, M., et al. 2023, *ApJS*, **265**, 5
- Harris, C. R., Millman, K. J., van der Walt, S. J., et al. 2020, *Natur*, **585**, 357
- Haslbauer, M., Kroupa, P., Zonoozi, A. H., & Hagi, H. 2022, *ApJL*, **939**, L31
- Hooper, D., & Goodenough, L. 2011, *PhLB*, **697**, 412
- Hunter, J. D. 2007, *CSE*, **9**, 90
- Ilie, C., Freese, K., Petric, A., & Paulin, J. 2023, arXiv:2312.13837
- Ilie, C., Freese, K., Valluri, M., Iliev, I. T., & Shapiro, P. R. 2012, *MNRAS*, **422**, 2164
- Ilie, C., Paulin, J., & Freese, K. 2023, *PNAS*, **120**, e2305762120
- Inayoshi, K., Harikane, Y., Inoue, A. K., Li, W., & Ho, L. C. 2022, *ApJL*, **938**, L10
- Iocco, F., Bressan, A., Ripamonti, E., et al. 2008, *MNRAS*, **390**, 1655
- Iocco, F., & Visinelli, L. 2024, *PDU*, **44**, 101496
- Jiao, H., Brandenberger, R., & Refregier, A. 2023, *PhRvD*, **108**, 043510
- Johnson, J. L. 2013, in *Astrophysics and Space Science Library*, Vol. 396, The First Galaxies, ed. T. Wiklind, B. Mobasher, & V. Bromm (Berlin: Springer), 177
- Kiziltan, B., Kottas, A., De Yoreo, M., & Thorsett, S. E. 2013, *ApJ*, **778**, 66
- Klessen, R. S., & Glover, S. C. O. 2023, *ARA&A*, **61**, 65
- Labbé, I., van Dokkum, P., Nelson, E., et al. 2023, *Natur*, **616**, 266
- Lewis, A., Challinor, A., & Lasenby, A. 2000, *ApJ*, **538**, 473
- Li, Z., Dekel, A., Sarkar, K. C., et al. 2024, *A&A*, **690**, A108
- Lin, H., Gong, Y., Yue, B., & Chen, X. 2024, *RAA*, **24**, 015009
- Lovell, C. C., Harrison, I., Harikane, Y., Tacchella, S., & Wilkins, S. M. 2022, *MNRAS*, **518**, 2511
- Madau, P., & Dickinson, M. 2014, *ARA&A*, **52**, 415
- Maurer, A., Raue, M., Kneiske, T., et al. 2012, *ApJ*, **745**, 166
- McLeod, D. J., Donnan, C. T., McLure, R. J., et al. 2024, *MNRAS*, **527**, 5004
- Menci, N., Adil, S. A., Mukhopadhyay, U., Sen, A. A., & Vagnozzi, S. 2024, *JCAP*, **2024**, 072
- Miralda-Escudé, J. 1998, *ApJ*, **501**, 15
- Morishita, T., & Stiavelli, M. 2023, *ApJL*, **946**, L35
- Murray, S. G., Power, C., & Robotham, A. S. G. 2013, *A&C*, **3**, 23
- Naidu, R. P., Oesch, P. A., van Dokkum, P., et al. 2022, *ApJL*, **940**, L14
- Natarajan, A., Tan, J. C., & O'Shea, B. W. 2009, *ApJ*, **692**, 574
- Nestí, F., Salucci, P., & Turini, N. 2023, *Astro*, **2**, 90
- Oguri, M., Diego, J. M., Kaiser, N., Kelly, P. L., & Broadhurst, T. 2018, *PRD*, **97**, 023518
- Oke, J. B., & Gunn, J. E. 1983, *ApJ*, **266**, 713
- Pérez-González, P. G., Costantin, L., Langeroodi, D., et al. 2023, *ApJL*, **951**, L1
- Planck Collaboration, Aghanim, N., Akrami, Y., et al. 2020, *A&A*, **641**, A6
- Qin, W., Muñoz, J. B., Liu, H., & Slatyer, T. R. 2024, *PhRvD*, **109**, 103026
- Reed, D. S., Bower, R., Frenk, C. S., Jenkins, A., & Theuns, T. 2007, *MNRAS*, **374**, 2
- Rieke, M., Robertson, B., Tacchella, S., et al. 2023, Data from the JWST Advanced Deep Extragalactic Survey (JADES), MAST, doi:10.17909/8TDJ-8N28
- Salpeter, E. E. 1955, *ApJ*, **121**, 161
- Sandick, P., Diemand, J., Freese, K., & Spolyar, D. 2011, *JCAP*, **2011**, 018
- Sandick, P., Diemand, J., Freese, K., & Spolyar, D. 2012, *PhRvD*, **85**, 083519
- Schleicher, D. R. G., Banerjee, R., & Klessen, R. S. 2009, *PhRvD*, **79**, 043510
- Scott, P., Venkatesan, A., Roebber, E., et al. 2011, *ApJ*, **742**, 129
- Somerville, R. S., & Davé, R. 2015, *ARA&A*, **53**, 51
- Su, B.-Y., Li, N., & Feng, L. 2023, arXiv:2306.05364
- Venditti, A., Bromm, V., Finkelstein, S. L., Graziani, L., & Schneider, R. 2024, *MNRAS*, **527**, 5102
- Virtanen, P., Gommers, R., Oliphant, T. E., et al. 2020, *NatMe*, **17**, 261
- Volonteri, M., Habouzit, M., & Colpi, M. 2021, *NatRP*, **3**, 732
- Wang, J. C., Huang, Z.-Q., Huang, L., & Liu, J. 2024, *RAA*, **24**, 045001
- Wang, P., Su, B.-Y., Zu, L., Yang, Y., & Feng, L. 2024, *EPJP*, **139**, 711
- Wang, Y. Y., Lei, L., Yuan, G.-W., & Fan, Y.-Z. 2023, *ApJL*, **954**, L48
- Wang, Z., Lei, L., Jiao, H., Feng, L., & Fan, Y.-Z. 2023, *SCPMA*, **66**, 120403
- Wechsler, R. H., & Tinker, J. L. 2018, *ARA&A*, **56**, 435
- Wu, Y., Baum, S., Freese, K., Visinelli, L., & Yu, H.-B. 2022, *PhRvD*, **106**, 043028
- Xiao, M., Oesch, P. A., Elbaz, D., et al. 2024, *Natur*, **635**, 311
- Yuan, G.-W., Lei, L., Wang, Y.-Z., et al. 2024, *SCPMA*, **67**, 109512
- Yuan, Q., Yue, B., Zhang, B., & Chen, X. 2011, *JCAP*, **2011**, 020
- Yung, L. Y. A., Somerville, R. S., Finkelstein, S. L., Wilkins, S. M., & Gardner, J. P. 2024, *MNRAS*, **527**, 5929
- Zackrisson, E., Scott, P., Rydberg, C.-E., et al. 2010a, *MNRAS*, **407**, L74
- Zackrisson, E., Scott, P., Rydberg, C.-E., et al. 2010b, *ApJ*, **717**, 257
- Zhang, S., Ilie, C., & Freese, K. 2024, *ApJ*, **965**, 121
- Zhou, B., Liang, Y.-F., Huang, X., et al. 2015, *PRD*, **91**, 123010
- Zhu, C. R., Cui, M.-Y., Xia, Z.-Q., et al. 2022, *PRL*, **129**, 231101